ALMA Millimeter/Submillimeter Sources among Spitzer SMUVS Galaxies at z > 2 in the COSMOS Field

Suzuki, Tomoko L.; van Mierlo, Sophie E.; Caputi, Karina I.

Published in:
Astrophysical Journal

DOI:
10.3847/1538-4357/ad023c

Publication date:
2023

The Astrophysical Journal, 959:82 (10pp), 2023 December 20 https://doi.org/10.3847/1538-4357/ad023c

ALMA Millimeter/Submillimeter Sources among Spitzer SMUVS Galaxies at $z > 2$ in the COSMOS Field

Tomoko L. Suzuki[1,2,3], Sophie E. van Mierlo[2], and Karina I. Caputi[2]
[1] Kavli Institute for the Physics and Mathematics of the Universe (WPI), The University of Tokyo Institutes for Advanced Study, The University of Tokyo, Kashiwa, Chiba 277-8583, Japan; tomoko.suzuki@ipmu.jp
[2] Kapteyn Astronomical Institute, University of Groningen, P.O. Box 800, 9700AV Groningen, The Netherlands
Received 2022 November 4; revised 2023 September 5; accepted 2023 September 5; published 2023 December 8

Abstract

Submillimeter observations reveal the star formation activity obscured by dust in the young Universe. It still remains unclear how galaxies detected at submillimeter wavelengths are related to ultraviolet/optical-selected galaxies in terms of their observed quantities, physical properties, and evolutionary stages. Deep near- and mid-infrared observational data are crucial to characterize the stellar properties of galaxies detected with submillimeter emission. In this study, we make use of a galaxy catalog from the Spitzer Matching survey of the UltraVISTA ultra-deep Stripes. By crossmatching with a submillimeter source catalog constructed with archival data of the Atacama Large Millimeter/submillimeter Array (ALMA), we search for galaxies at $z > 2$ with a submillimeter detection in our galaxy catalog. We find that the ALMA-detected galaxies at $z > 2$ are systematically massive and have redder K_s–[4.5] colors than the nondetected galaxies. The redder colors are consistent with the larger dust reddening values of the ALMA-detected galaxies obtained from spectral energy distribution (SED) fitting. We also find that the ALMA-detected galaxies tend to have brighter 4.5 μm magnitudes. This may suggest that they tend to have smaller mass-to-light ratios and thus to be younger than star-forming galaxies fainter at submillimeter wavelengths with similar stellar masses. We identify starburst galaxies with high specific star formation rates among both ALMA-detected and nondetected SMUVS sources. Irrespective of their brightness at submillimeter wavelengths, these populations have similar dust reddening values, which may suggest a variety of dust SED shapes among the starburst galaxies at $z > 2$.

Unified Astronomy Thesaurus concepts: High-redshift galaxies (734); Submillimeter astronomy (1647); Galaxy evolution (594)

1. Introduction

Star formation in galaxies is accompanied by dust production, and the ultraviolet (UV) light from young and massive stars in star formation regions is absorbed by dust and re-emitted as thermal emission at infrared (IR) wavelengths. It is crucial to trace both the dust-obscured and unobscured components of the galaxy spectrum in order to account for the total star formation activity in galaxies in an unbiased way. The fraction of dust-obscured star formation in the cosmic star formation rate (SFR) density is said to increase with redshifts up to $z \sim 2$ (see, e.g., Takeuchi et al. 2005; Burgarella et al. 2013, and Madau & Dickinson 2014). Furthermore, recent submillimeter observations suggest that ~40%–50% of the total star-forming activity is obscured by dust at higher redshifts, such as $z \sim 3$–4 (e.g., Bouwens et al. 2016; Zavala et al. 2021) or even out to $z \sim 7$ (Algera et al. 2023). The dust-obscured star formation is considered to play an important role in galaxy formation and evolution across cosmic time.

Submillimeter bright galaxies (SMGs) were first identified with submillimeter observations with single-dish telescopes, and their observed flux densities at ~850 μm–1 mm are typically larger than a few millijansky (e.g., Smail et al. 1997; Barger et al. 1998; Hughes et al. 1998). Follow-up observations with high angular resolutions using large radio interferometers, such as the Atacama Large Millimeter/submillimeter Array (ALMA), allow us to pin down the positions of SMGs on the sky and thus make it easier to find their optical counterparts. With the multiwavelength photometric information from optical to radio, the physical properties of SMGs have been characterized (e.g., Hodge et al. 2013; da Cunha et al. 2015; Michałowski et al. 2017; Miettinen et al. 2017; An et al. 2018, 2019; Dudzevičiūtė et al. 2020). SMGs are said to be typically massive ($\log(M_*/M_\odot) > 10$) and have high SFRs of a few 100–1000 $M_\odot\,\mathrm{yr}^{-1}$ (see Hodge & da Cunha 2020 for a recent review). Furthermore, deep blind surveys (e.g., Dunlop et al. 2017; Aravena et al. 2020; Franco et al. 2020; Yamaguchi et al. 2020) or individual observation programs targeting UV/optical-selected galaxies (e.g., Schinnerer et al. 2016; Scoville et al. 2016; Tadaki et al. 2020) with ALMA reveal a population of galaxies with fainter submillimeter fluxes of $\lesssim$1 mJy. Such relatively submillimeter faint galaxies are also typically massive with $\log(M_*/M_\odot) > 10$ and have SFRs of $\gtrsim 30\,M_\odot\,\mathrm{yr}^{-1}$.

A systematic comparison between submillimeter-detected galaxies and UV/optical-selected galaxies at the same epoch is crucial to understand what galaxy populations are traced by the submillimeter observations and what is the role of such submillimeter-detected galaxies on galaxy formation and evolution at high redshifts in a broader context. Deep near-infrared (NIR) and mid-infrared (MIR) photometric data are required to estimate the stellar properties of submillimeter-detected galaxies at high redshifts accurately, given their strong dust extinction (e.g., An et al. 2019; Dudzevičiūtė et al. 2020;

[3] Canon Foundation in Europe Research Fellow.

Franco et al. 2020; Yamaguchi et al. 2020). This makes it possible to compare submillimeter-detected galaxies and relatively submillimeter faint galaxies systematically. The Spitzer Matching survey of the UltraVISTA ultra-deep Stripes (SMUVS; PI: Caputi; Ashby et al. 2018, 2020) is a Spitzer (Werner et al. 2004) Exploration Science Program with the Infrared Array Camera (IRAC; Fazio et al. 2004). SMUVS conducted ultradeep 3.6 and 4.5 μm imaging observations in part of the COSMOS field (Scoville et al. 2007; COSMOS Project 2020). The survey area is matched with that covered by the UltraVISTA ultradeep NIR imaging observations (McCracken et al. 2012), as well as the ultradeep Subaru imaging (Taniguchi et al. 2007). The point-source sensitivity of the IRAC 3.6 and 4.5 μm channels in SMUVS reaches down to 25 mag with 4σ significance (Ashby et al. 2018). The widefield and deep Spitzer/IRAC data from SMUVS enable us to construct a stellar-mass-selected galaxy sample at $z > 2$ (Deshmukh et al. 2018), which is expected to be insensitive to the presence of dust obscuration in galaxies. The SMUVS galaxy sample is suitable to systematically investigate the physical properties of dusty and nondusty galaxies at high redshifts once the observational data at far-IR and/or submillimeter wavelengths are available.

In this study, we combined the SMUVS galaxy catalog with a public submillimeter source catalog constructed with ALMA archival data in the COSMOS field (A^{3}COSMOS; Liu et al. 2019) to investigate the dust-obscured star formation activities of galaxies in the SMUVS catalog. At the same time, we also searched for SMUVS sources located on ALMA maps but having no counterpart in the A^{3}COSMOS catalog. By constructing two samples of galaxies both detected and undetected at submillimeter wavelengths, we aim to conduct a systematic comparison between submillimeter bright and submillimeter faint galaxies at the same epoch.

This paper is organized as follows: in Section 2, we describe the galaxy catalog obtained by SMUVS briefly and explain the counterpart search for the SMUVS sources at $z > 2$ in a submillimeter source catalog. In Section 3, we explain our stacking analysis for the ALMA nondetected sources and the spectral energy distribution (SED) fitting analysis with the multiwavelength data from optical to submillimeter. We show our results and discuss the difference between the ALMA-detected and nondetected SMUVS sources at $z > 2$ in Section 4. In Section 5, we summarize the main findings of this study. Throughout this paper, we use the cosmological parameters of $H_0 = 70\,\mathrm{km\,s^{-1}\,Mpc^{-1}}$, $\Omega_\mathrm{m} = 0.3$, and $\Omega_\Lambda = 0.7$. We assume a Chabrier (2003) initial mass function (IMF). Magnitudes are given in the AB system (Oke & Gunn 1983).

2. ALMA Counterpart Search for SMUVS Galaxies

2.1. SMUVS Galaxy Catalog

The source detection and photometry of the SMUVS sources were described in Deshmukh et al. (2018). The source detection in SMUVS was primarily done with UltraVISTA data release 3 (DR3) HK$_s$ stack maps. At the positions of the detected sources in the HK$_s$ images, the photometry on the SMUVS 3.6 and 4.5 μm mosaics was obtained with a point-spread function (PSF) fitting technique using the DAOPHOT package on IRAF. When the photometry was not successfully obtained with this PSF fitting technique, the fluxes of the IRAC channels are measured with a 2.″4 diameter circular aperture at the positions of the HK$_s$ stack maps and then converted to the total fluxes by multiplying the aperture fluxes by a factor of 2.13. The sources detected in at least one IRAC channel are referred as the "SMUVS sources" (Deshmukh et al. 2018). There are a total of ~300,000 SMUVS galaxies over 0.66 deg^2.

In this work, we use a newer version of the SMUVS catalog, which includes updated UltraVISTA photometry from DR4. van Mierlo et al. (2022) conducted the SED fitting for the SMUVS sources with the SED fitting code LEPHARE (Arnouts et al. 1999; Ilbert et al. 2006). They used the following photometric information available in the COSMOS field together with IRAC 3.6 and 4.5μm data from SMUVS: the CFHT u band; Subaru B, V, r, i_p, z_p, z_{pp}, IA427, IA464, IA484, IA505, IA527, IA624, IA679, IA709, IA738, IA767, IA827, NB711, and NB816; Hubble Space Telescope F814W; and UltraVISTA Y, J, H, and K_s. The fluxes of these 26 bands were measured with a 2″ diameter aperture and then converted to the total fluxes by applying point-source aperture corrections in each band (Deshmukh et al. 2018; van Mierlo et al. 2022). Because the source detection and photometry in SMUVS are optimized mainly for galaxies at $z > 2$, we focus on galaxies at $z > 2$. In the following analysis, we use the photometric redshifts, stellar masses, and dust reddening values $E(B-V)$ of the best-fit SEDs obtained from LEPHARE.

2.2. Submillimeter Counterpart Search with A^{3}COSMOS Catalog

We use a public submillimeter source catalog from the A^{3}COSMOS project[4] (Liu et al. 2019) to search for SMUVS sources at $z > 2$ with ALMA counterparts. The A^{3}COSMOS catalog is constructed with the ALMA archival data in the COSMOS field. We used the submillimeter source catalog with the version of 20180801. There are two public catalogs of the continuum sources, namely the blind source catalog and the prior source catalog. We combined the two source catalogs by matching the coordinates with a 1″ searching radius, as done in Liu et al. (2019). Then we conducted the crossmatch with the SMUVS catalog by using the coordinates in the A^{3}COSMOS prior source catalog for the submillimeter sources. In this study, we focused on the submillimeter sources detected at Band 6 (~1.2 mm) or Band 7 (~870 μm). As a result of crossmatching with a matching radius of 1″, we found 157 SMUVS sources at $z > 2$ that have at least one counterpart in the A^{3}COSMOS catalog. The median separation between the coordinates from the SMUVS and A^{3}COSMOS catalog is 0.″17. The separation is smaller than 0.″4 for 90% of the crossmatched sources. We also visually checked whether the dust continuum emission is spatially associated to the stellar continuum emission with the ALMA maps and the *Ks*-band images from UltraVISTA DR4. We confirmed that the searching radius of 1″ is reasonable for the counterpart search.

In the following, we use the total flux in the A^{3}COSMOS prior source catalog. When the sources were observed with the same band at least twice in different observing programs, we used the information with the closest separation from the SMUVS positions. Among 157 SMUVS sources with at least one A^{3}COSMOS counterpart, 22 sources were detected with both Band 6 and 7. Furthermore, six sources are detected with other bands, such as Bands 3, 4, or 8, as well.

[4] https://sites.google.com/view/a3cosmos/home?authuser=0

2.3. SMUVS Sources without A^{3}COSMOS Counterpart

We searched for the SMUVS sources at $z = 2.0$–5.5 that are covered by the ALMA maps in the A^{3}COSMOS catalog but have no counterpart in the A^{3}COSMOS catalog. These SMUVS sources can be regarded as galaxies with fainter submillimeter continuum flux as compared to the sources with A^{3}COSMOS counterparts. The areal coverage of the ALMA maps in A^{3}COSMOS is 79.5 arcmin^2 and 54.7 arcmin^2 for Band 6 and Band 7, respectively (Liu et al. 2019). Because the outer region in an ALMA map has lower sensitivity due to the primary beam attenuation, we consider only the SMUVS sources in the inner regions where the primary beam response is greater than 0.5. This leads to the exclusion of the sources that are not detected with dust emission due to shallow sensitivity limits. We also removed the ALMA maps with smaller beam sizes of $b_{\rm maj} \lesssim 0\farcs6$ in order to ensure that the given upper limits based on the rms level per beam can be compared with the total submillimeter fluxes of the ALMA-detected sources. When a source was observed multiple times with the same band, we used the map with the smallest rms level.

We measured the aperture fluxes of the SMUVS sources without a counterpart in the A^{3}COSMOS catalog for a stacking analysis (see Section 3.1 for more detailed explanation). We used the ALMA maps selected as mentioned above and measured the fluxes at the positions of the SMUVS sources with a $1\farcs5$ radius aperture. We found that two sources have an aperture flux with a signal-to-noise ratio (S/N) $\geqslant 3$ and that the submillimeter continuum emission is spatially associated to the *Ks*-band images, which means that these sources can be regarded as detected at submillimeter wavelengths. One source has a counterpart in the A^{3}COSMOS prior catalog only, and thus it was not identified in our counterpart search described in Section 2.2, which requires a detection in both the prior and blind source catalog. The other source is not included in either the A^{3}COSMOS prior or blind source catalogs, probably due to the faintness of the submillimeter flux and/or the NIR flux used for the prior fit in Liu et al. (2019). We add the two sources to the sample of the ALMA-detected SMUVS sources and use the aperture fluxes as the total fluxes in the following analysis.

2.4. Sample of SMUVS Galaxies Detected/Nondetected with ALMA

We crossmatched the ALMA-detected and nondetected SMUVS sources with spectroscopic redshift catalogs available in the COSMOS field (e.g., Lilly et al. 2007; Comparat et al. 2015; Kriek et al. 2015; Le Fèvre et al. 2015; Hasinger et al. 2018). We found 11 ALMA-detected and 62 nondetected SMUVS sources with spectroscopic redshifts. We then evaluated the photometric redshift accuracy of the two samples with the fraction of outliers, which are defined as $\sigma = |z_{\rm spec} - z_{\rm phot}|/(1 + z_{\rm spec}) \geqslant 0.15$, and the normalized median absolute deviation (MAD), the median of σ multiplied by 1.48 (Laigle et al. 2016). The ALMA-detected SMUVS sources have an outlier fraction of 18% and $\sigma_{\rm MAD} = 0.051$. As for the nondetected SMUVS sources, the outlier fraction is 15% and $\sigma_{\rm MAD} = 0.035$. Both the outlier fraction and $\sigma_{\rm MAD}$ are similar between the ALMA-detected and nondetected SMUVS sources, which means that the accuracy of the photometric redshifts from the SMUVS survey does not strongly depend on the submillimeter brightness.

Table 1
The Number of SMUVS Sources at $z = 2.0$–5.5 with and without ALMA Detection

ALMA Detection	Band 6 (∼1.2 mm)	Band 7 (∼870 μm)	Total
Yes	97	68	145
No	1309	637	1859

Note. Among 145 ALMA-detected SMUVS sources, 20 sources are detected with both Bands 6 and 7. As for the nondetected SMUVS sources, 87 sources have the flux upper limit in both Bands 6 and 7.

We also crossmatched our samples with the Chandra X-ray point-source catalog (Civano et al. 2016). Nine ALMA-detected and 27 nondetected SMUVS sources have X-ray counterparts and among them, three and nine sources, respectively, have spectroscopic redshifts too. It turned out that two out of the three ALMA-detected sources with X-ray counterparts and six out of the nine nondetected sources with X-ray counterparts were classified as photometric redshift outliers. These sources are at $z_{\rm spec} < 2$, and thus are active galactic nuclei (AGNs) at lower redshift. This indicates that the SMUVS sources with X-ray counterparts are more likely to be AGNs at $z < 2$. Given the possibility that the SED fitting with galaxy templates would not work well for X-ray AGNs, even for ones with the correct photometric redshifts, we decided to remove all the X-ray sources in the following analysis. We removed the photo-z outliers with no X-ray counterpart as well.

After removing the photo-z outliers and X-ray-detected sources, the number of ALMA-detected and nondetected SMUVS sources become 150 and 1859, respectively. Moreover, as explained in detail in Section 3.2, we removed five ALMA-detected SMUVS sources that are considered to be poorly fitted with MAGPHYS. The number of galaxies in each sample used in the following analysis is summarized in Table 1. We assigned 4.2σ upper limits on the submillimeter fluxes of the SMUVS sources without ALMA detection, according to the detection limit of 4.2σ for the prior source catalog in Liu et al. (2019).

Figure 1 shows the stellar mass of the ALMA-detected and nondetected SMUVS sources at $z = 2.0$–5.5 as a function of redshift. The top and right histograms show comparisons of the redshift and stellar-mass distributions of the two samples, respectively. We note that the stellar masses shown in Figure 1 come from the best-fit SEDs obtained from LEPHARE (van Mierlo et al. 2022). Whereas the ALMA-detected and nondetected SMUVS sources have a similar redshift distribution, the ALMA-detected sources are systematically more massive ($\log(M_*/M_\odot) > 10$) as compared to the nondetected sources. The median stellar mass of the ALMA-detected and nondetected SMUVS sources is $\log(M_*/M_\odot) = 10.51$ and 9.40, respectively. This trend is expected, because previous submillimeter observations show that the galaxy selection based on submillimeter brightness preferentially picks up massive star-forming galaxies (e.g., da Cunha et al. 2015; Dunlop et al. 2017; Dudzevičiūtė et al. 2020; Yamaguchi et al. 2020). In Figure 2, we show the flux (upper limit) at 1.2 mm and 870 μm of the ALMA-detected and nondetected SMUVS sources as a function of stellar mass at $z = 2.0$–3.0 and at $z = 3.0$–5.5, separately. The nondetected SMUVS sources have reasonable upper limits on their continuum fluxes as compared to the dust continuum fluxes of the individually detected

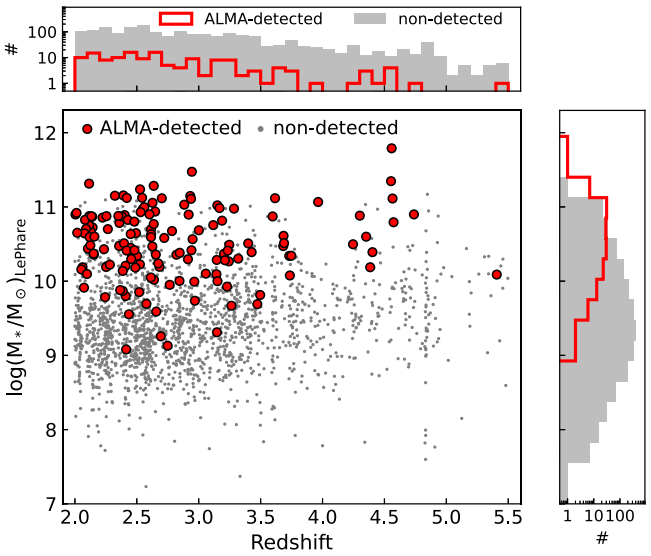

Figure 1. Stellar mass of the ALMA-detected and nondetected SMUVS sources analyzed in this study as a function of redshift. The stellar masses and redshifts of both the ALMA-detected and nondetected sources are from the best-fit SEDs obtained from LEPHARE with the 28 band photometry from u band to 4.5 μm (van Mierlo et al. 2022). ALMA-detected sources are at the high-mass end of the mass distribution of the nondetected SMUVS sources, whereas there is no clear difference between the redshift distributions of the two samples.

sources at a given stellar mass. We note that the ALMA nondetected SMUVS sources include not only submillimeter faint star-forming galaxies, but also galaxies with little star formation, because we do not apply any cut on the star formation activity of galaxies.

3. Analysis

3.1. Stacking Analysis for the Nondetected Sources

We conducted a stacking analysis for the SMUVS sources without an ALMA counterpart to investigate their average submillimeter fluxes. Because the pixel scales and beam sizes vary between ALMA maps from different projects, we decided to follow the stacking method with aperture fluxes applied in Fudamoto et al. (2020), who conducted a stacking analysis with the ALMA maps in the A^{3}COSMOS catalog. As a test, we measured the aperture fluxes of the ALMA-detected SMUVS sources and confirmed that the aperture fluxes show a good agreement with the total fluxes in the A^{3}COSMOS catalog when they are isolated. We conducted this test by changing the aperture radius, namely $r = 1\farcs0$, $1\farcs5$, and $2\farcs0$. The consistency with the total fluxes in the A^{3}COSMOS catalog does not change depending on the aperture size. Here we use $r = 1\farcs5$ apertures.

We divided the nondetected SMUVS sources at $z = 2.0$–5.5 with $\log(M_*/M_\odot) \geqslant 9.0$ into 18 subsamples according to their stellar masses, redshifts, and the observed wavelengths (Band 6 or 7), as summarized in Table 2. We measured the ALMA aperture fluxes of each nondetected source at the position from the SMUVS catalog. We use the ALMA maps before the primary beam correction released by the A^{3}COSMOS project.[5] The errors on the aperture fluxes are determined from the standard deviation of the aperture fluxes measured at 100 random positions on each ALMA map.

Before stacking, we removed the SMUVS sources that have a close submillimeter bright source that contaminates their aperture fluxes. We also removed passive galaxies, which are considered to be intrinsically faint at submillimeter wavelength, in order to increase the S/N of the stacking result. We followed the method applied in Deshmukh et al. (2018) to distinguish passive galaxies from star-forming galaxies. Deshmukh et al. (2018) divided the SMUVS galaxy sample at $z > 2$ into subsamples of passive galaxies, dusty star-forming galaxies, and nondusty star-forming galaxies, based on the rest-frame $u - r$ color and $E(B - V)$. According to their criteria, the nondetected SMUVS sources with $(u - r)_{\rm rest} > 1.3$ and $E(B - V) < 0.2$ were classified as passive galaxies and removed from the stacking analysis. The fraction of such sources is 5%.

When we stacked the aperture fluxes for each subsample, the aperture fluxes were weighted according to the rms values after correcting for the primary beam attenuation at the position of the sources (Fudamoto et al. 2020). Errors on the stacked fluxes were estimated with the jackknife resampling method (e.g., Efron 1982). We generated N samples with a sample size of $N - 1$ from an SMUVS subsample with the size of N. The ith source was removed from the ith jackknife sample. Then we calculated a stacked flux for each jackknife sample in the same manner as done for the SMUVS subsamples. We use the standard deviation of the stacked fluxes of the jackknife samples as an error on the stacked flux of the SMUVS subsample.

Table 2 summarizes the results of the stacking analysis. Four out of the 18 subsamples show stacked continuum fluxes with S/N > 3. As expected, subsamples consisting of galaxies with higher stellar masses and at lower redshift tend to have higher S/N. The remaining subsamples show the stacked fluxes with $<3\sigma$, such that we adopt 3σ flux upper limits for them. The relation between the stacked fluxes and stellar masses of the 18 subsamples is shown in Figure 2. The stacking-detected subsamples have $\sim$ 1 dex fainter fluxes as compared to the individually detected SMUVS sources with similar stellar masses. The comparison between the stacked subsamples and individually detected sources would indicate the large scatter of submillimeter continuum fluxes of star-forming galaxies even at the same stellar mass.

3.2. SED Fitting with MAGPHYS

We conducted an independent SED fitting of the ALMA-detected SMUVS sources in order to take into account their stellar and dust emission properties simultaneously. We used an SED fitting code MAGPHYS that can fit SEDs from the optical to radio wavelengths consistently (da Cunha et al. 2008, 2015; Battisti et al. 2020).

MAGPHYS uses the stellar population synthesis models of Bruzual & Charlot (2003), assuming a Chabrier (2003) IMF, and it uses the two-component dust model of Charlot & Fall (2000) for the dust attenuation. The metallicity range is set to be 0.2–2.0$\times Z_\odot$, and the age range is 0.1–10 Gyr. The star formation history is parameterized as a continuous delayed exponential function, in which the SFR rises linearly at the earlier epoch and then declines exponentially with the timescale defined by the γ parameter ($\gamma = 0.075$–1.5 Gyr^{-1}). MAGPHYS also includes starbursts of random duration and amplitude to account for stochastic star formation. We used the

[5] https://irsa.ipac.caltech.edu/data/COSMOS/overview.html

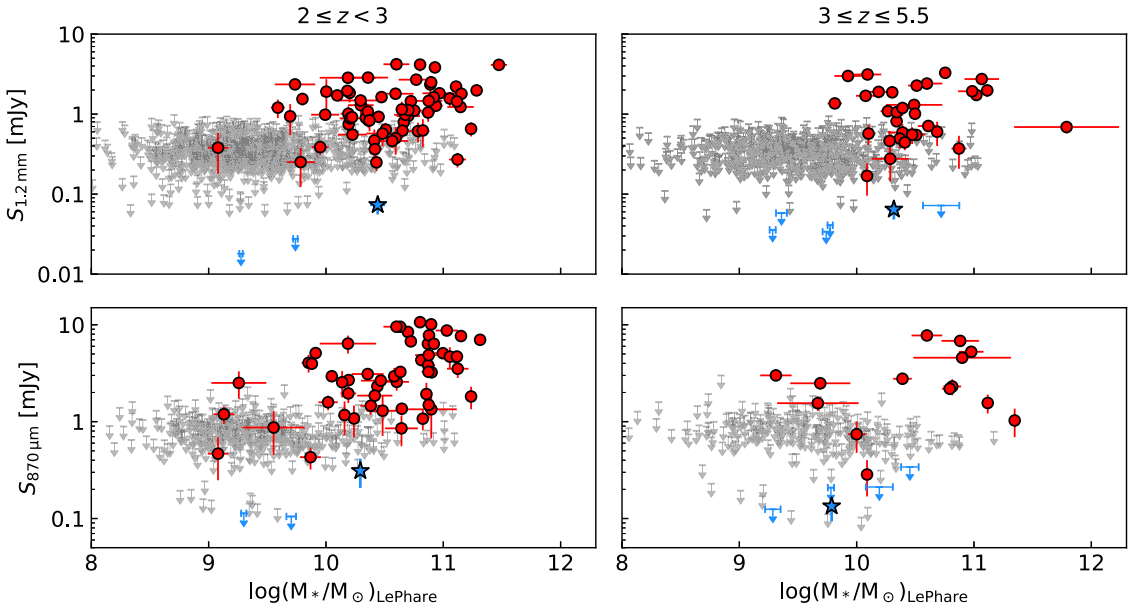

Figure 2. Continuum flux (upper limit) at ∼1.2 mm (top) and ∼870 μm (bottom) as a function of stellar mass of the SMUVS sources in the two redshift bins, namely $z = 2.0$–3.0 (left) and $z = 3.0$–5.5 (right), analyzed in this study. As for the nondetected SMUVS sources, we show 4.2σ upper limits after correcting for the primary beam attenuation (Liu et al. 2019). The nondetected SMUVS sources have reasonable upper limits on their continuum fluxes as compared to the individually detected SMUVS sources. The results of the stacking analysis for the nondetected sources are also shown with star symbols and arrows (Section 3.1).

MAGPHYS high-z extension version 2, which includes the 2175 Å feature in the dust attenuation curve (Battisti et al. 2020). The high-z extension version 2 uses the intergalactic medium absorption in the UV regime from Inoue et al. (2014).

We combined the submillimeter detection(s) from ALMA with the broadband photometry from the SMUVS catalog (van Mierlo et al. 2022). For bands in the optical to NIR regime, we inspect the S/N in each band, such that if the S/N <3, we instead adopt a 3σ flux upper limit in that band. Redshifts are fixed to the photometric redshifts in the SMUVS catalog.

In order to maximize the constraints on the IR SEDs, we added photometric information in the IR regime other than the ALMA data. We used the IR photometric catalog constructed by Jin et al. (2018). This catalog contains multiwavelength photometry ranging from Spitzer/IRAC 3.6 μm to Karl G. Jansky Very Large Array 1.4 GHz, measured with the "super-deblending" technique developed by Liu et al. (2018). We crossmatched the coordinates of the ALMA-detected SMUVS sources with those of the sources in the super-deblended catalog of Jin et al. (2018) with a searching radius of 1″. Most of the ALMA-detected SMUVS sources (∼90%) have a counterpart in the super-deblended catalog. We added the photometric information from Spitzer/IRAC 5.8 μm to Herschel/SPIRE 500 μm to the photometric catalog of the ALMA-detected SMUVS sources. When the S/N < 3, 3σ upper limits were assigned.

In order to evaluate the goodness of the fits obtained with MAGPHYS, we adopt the criterion introduced by Battisti et al. (2019). They classify the sources that failed to fit based on their best-fit χ^2 values. They fit a Gaussian distribution to the lower 90 % population of a sample and determine the mean ($\bar{\chi}^2$) and dispersion ($\sigma(\chi^2)$). When $\chi^2 > \bar{\chi}^2 + 4\sigma(\chi^2)$, the sources are considered to be poorly fitted. We found that five sources in our sample have a χ^2 value exceeding this criterion. The five sources are removed in the following analysis.

Figure 3 shows the comparison of the stellar masses from LEPHARE and MAGPHYS of the ALMA-detected SMUVS sources at $z = 3.0$–5.5. We find that the stellar masses from MAGPHYS are systematically larger than those from LEPHARE. This effect was also shown in Battisti et al. (2019; see also Michałowski et al. 2014). The difference between the two stellar-mass measurements is ∼0.25 dex on average.

We also conducted the SED fitting with MAGPHYS for the four stacked subsamples with a detection of >3σ (Section 3.1). In the following analysis, we use the median IR luminosities obtained with MAGPHYS to investigate the dust-obscured star formation activities of the ALMA-detected SMUVS sources and the four stacking-detected subsamples. As for the stellar mass, we use the values obtained from LEPHARE for consistency between the ALMA-detected and nondetected sources.

3.3. SFRs

The absolute UV magnitudes at rest-frame 1450 Å from LEPHARE are available for all the SMUVS sources. We calculated SFRs from the rest-frame UV luminosities ($\mathrm{SFR_{UV}}$) with the following equation from Kennicutt (1998), scaled to a Chabrier (2003) IMF:

$$\mathrm{SFR_{UV}}\,[M_\odot \mathrm{yr}^{-1}] = 8.8 \times 10^{-29}\, L_\nu\,[\mathrm{erg\ s^{-1}\ Hz^{-1}}], \quad (1)$$

where L_ν is the luminosity at 1450 Å. As for the nondetected SMUVS sources, we calculated SFR_{UV} after correcting for the dust extinction using $E(B-V)$ from LEPHARE and the Calzetti et al. (2000) attenuation law. In the following analysis, we used the dust-extinction-corrected SFR_{UV} as the total SFR for the nondetected SMUVS sources. To estimate errors on $\mathrm{SFR_{UV}}$, we used the uncertainties on the observed fluxes close to 1450 Å in the rest frame.

In the case of the ALMA-detected sources, we estimated the SFRs by combining the SFRs from the rest-frame UV

Table 2
Summary of the Stacking Analysis for the Nondetected SMUVS Sources at $z = 2.0$–5.5

Bins		Band 6 (1.2 mm)				Band 7 (870 μm)			
z	$\log(M_*/M_\odot)$	#	Stacked Flux (mJy)	z	$\log(M_*/M_\odot)$	#	Stacked Flux (mJy)	z	$\log(M_*/M_\odot)$
2.0–3.0	>10.0	83	0.073 ± 0.018	2.49 ± 0.05	10.44 ± 0.06	49	0.31 ± 0.10	2.34 ± 0.06	10.29 ± 0.03
	9.5–10.0	178	<0.028	2.55 ± 0.04	9.74 ± 0.02	89	<0.105	2.53 ± 0.06	9.70 ± 0.04
	9.0–9.5	294	<0.018	2.48 ± 0.03	9.28 ± 0.01	148	<0.113	2.46 ± 0.04	9.30 ± 0.02
3.0–4.0	>10.0	49	0.064 ± 0.016	3.45 ± 0.09	10.32 ± 0.05	30	<0.341	3.71 ± 0.06	10.45 ± 0.07
	9.5–10.0	117	<0.041	3.39 ± 0.05	9.77 ± 0.02	45	<0.209	3.54 ± 0.07	9.78 ± 0.03
	9.0–9.5	124	<0.036	3.46 ± 0.06	9.28 ± 0.03	48	<0.125	3.56 ± 0.09	9.29 ± 0.07
4.0–5.5	>10.0	19	<0.072	4.88 ± 0.11	10.72 ± 0.15	16	<0.212	5.31 ± 0.17	10.19 ± 0.11
	9.5–10.0	47	<0.034	4.57 ± 0.05	9.74 ± 0.03	26	0.134 ± 0.041	4.66 ± 0.25	9.79 ± 0.03
	9.0–9.5	38	<0.058	4.70 ± 0.14	9.36 ± 0.05			…	

Note. When $S/N < 3$, the 3σ upper limits are assigned. The redshifts and stellar masses of the subsamples are estimated by taking a weighted average, as done for the aperture fluxes.

luminosities and IR luminosities (e.g., Wuyts et al. 2011; Yamaguchi et al. 2020). IR luminosities are converted to SFR_{IR} with the Kennicutt (1998) prescription scaled to a Chabrier (2003) IMF and combined with SFR_{UV} before dust extinction correction, as follows:

$$SFR_{UV+IR}\,[M_\odot yr^{-1}] = SFR_{UV,dust\ uncorr} + 1.09 \times 10^{-10}\, L_{IR}\,[L_\odot], \quad (2)$$

where L_{IR} is a median IR luminosity obtained from MAGPHYS (Section 3.2). The errors on SFR_{IR} are estimated using the 16th and 84th percentiles of the L_{IR} obtained from MAGPHYS.

4. Results and Discussion

4.1. NIR/MIR Brightness and Colors

Figure 4 shows the comparison of the observed quantities—namely the *Ks*-band magnitude, 4.5 μm magnitude, and *Ks*–[4.5] color—between the ALMA-detected and nondetected SMUVS sources at $z = 2.0$–5.5. We here gave a weight to each nondetected SMUVS source according to its stellar mass, so that the weighted stellar-mass distribution of the nondetected sources matches with the stellar-mass distribution of the ALMA-detected sources. By using the weighted distribution of the nondetected sources for comparison, we can minimize the effect of the stellar-mass dependency of each quantity.

The ALMA-detected and nondetected SMUVS sources at $z = 2.0$–5.5 have similar *Ks*-band magnitude distributions. On the other hand, the 4.5 μm magnitude distribution of the ALMA-detected SMUVS sources appears to be shifted toward brighter magnitudes as compared to that of the nondetected sources. When comparing the *Ks*–[4.5] color distribution between the two samples, the ALMA-detected SMUVS sources tend to have redder colors of *Ks*–[4.5] $\gtrsim 1$.

Colors in the NIR and Spitzer/IRAC bands are used to select (extremely) dusty galaxies at high redshift (e.g., Wang et al. 2012, 2016; Chen et al. 2016). Wang et al. (2012) selected extremely red objects based on the *Ks*–[4.5] colors (KIEROs; *Ks*–[4.5] >1.6) and showed that the majority of KIEROs are massive ($\log(M_*/M_\odot) =$ 10–12) star-forming galaxies at $z = 2$–4. Of the ALMA-detected SMUVS sources, 44% have *Ks*–[4.5] > 1.6 and 46% have bluer colors of *Ks*–[4.5] = 1.0–1.6. Half of them are not as extremely red as KIEROs. These results suggest that the *Ks*–[4.5] color is useful to select galaxies bright at submillimeter wavelengths at $z > 2$, and that applying a cut at *Ks*–[4.5] ~1 would lead to an increase in completeness.

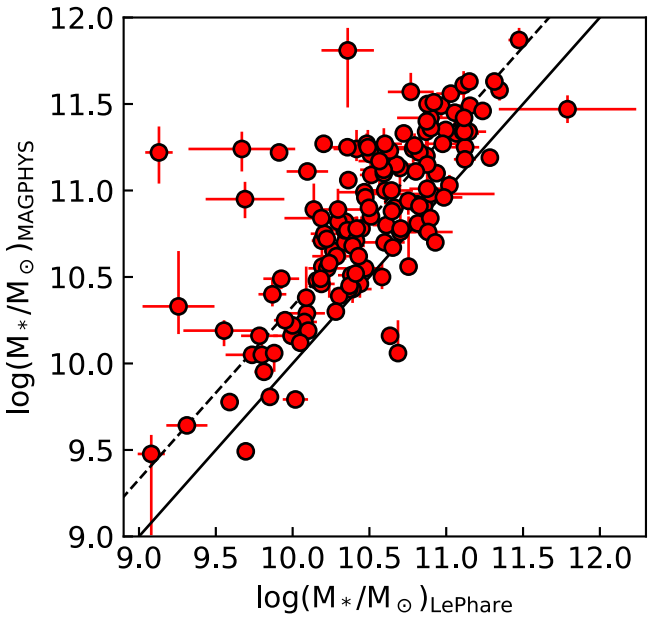

Figure 3. Comparison of the stellar masses obtained from LEPHARE and MAGPHYS for the ALMA-detected SMUVS sources at $z = 2.0$–5.5. The solid line represents the identity line. The dashed line represents the case when the stellar mass from MAGPHYS is 0.25 dex larger than that from LEPHARE. The stellar masses from MAGPHYS are systematically larger than those from LEPHARE.

As shown in the next section, we find that the dust reddening values, $E(B-V)$, of the ALMA-detected SMUVS sources are systematically larger than those of the nondetected sources. The observed redder *Ks*–[4.5] colors of the ALMA-detected SMUVS sources appear to be consistent with their stronger dust extinction (Wang et al. 2012). On the other hand, the trends of the *Ks*-band and 4.5 μm magnitude distributions shown in Figure 4 seem to be difficult to explain only with the different dust extinction strengths between the two samples. Brighter 4.5 μm magnitudes of the ALMA-detected SMUVS sources may suggest that galaxies with bright submillimeter emission tend to have smaller mass-to-light ratios at $\lambda_{obs} = 4.5$ μm, and

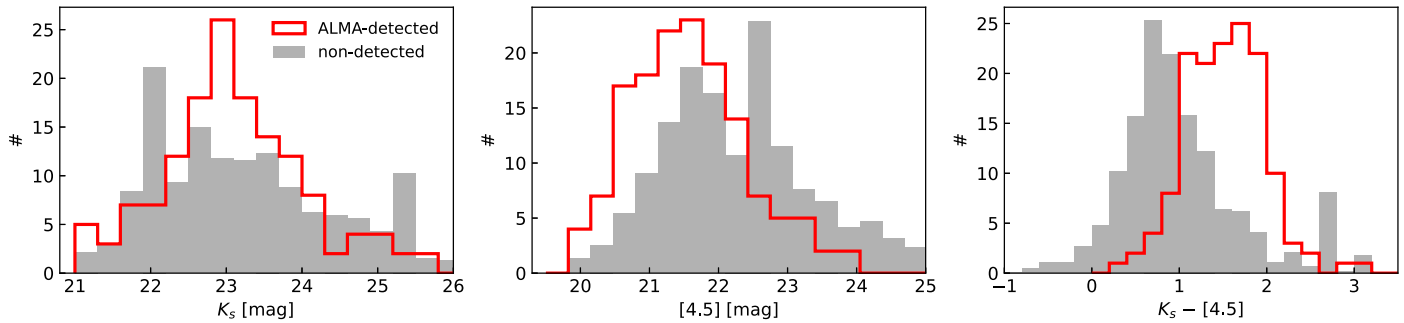

Figure 4. Comparison of *Ks*-band magnitude, 4.5 μm magnitude, and *Ks*–[4.5] color between the ALMA-detected and nondetected SMUVS sources at $z = 2.0$–5.5. The histograms of the nondetected SMUVS sources are weighted according to the stellar masses so that the stellar-mass distribution becomes the same between the ALMA-detected and nondetected sources. The ALMA-detected sources at $z \geqslant 2$ tend to be brighter at 4.5 μm and have systematically redder *Ks*–[4.5] colors than the nondetected sources, even when considering the difference of the stellar-mass distributions.

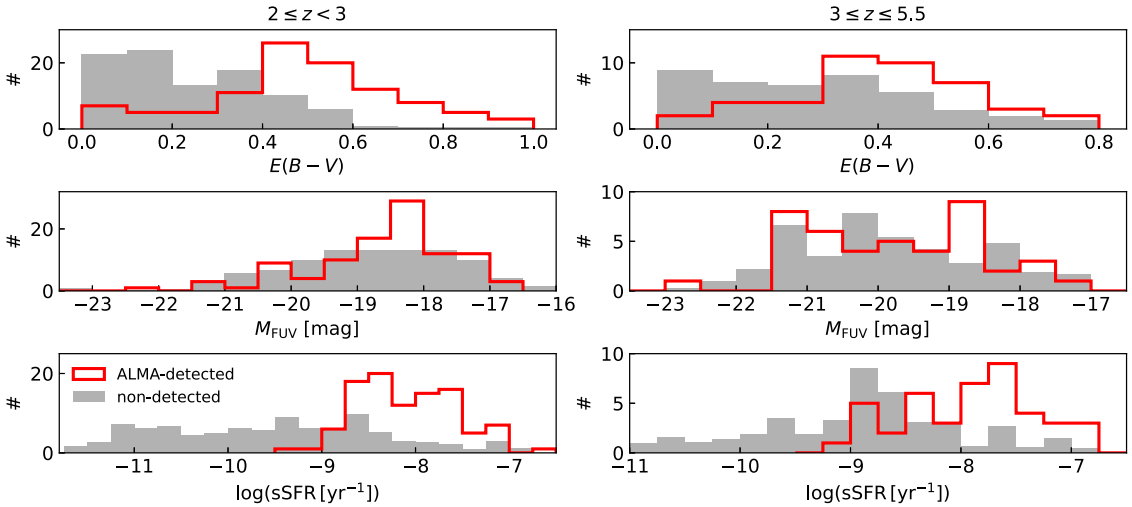

Figure 5. Comparison of the physical quantities between the ALMA-detected and nondetected SMUVS sources at $z = 2.0$–3.0 (left) and $z = 3.0$–5.5 (right). Here, the nondetected SMUVS sources are weighted according to their stellar masses, as done in Figure 4. The ALMA-detected sources tend to be dustier and more active in star formation than the nondetected sources.

thus tend to be younger as compared to those fainter at submillimeter wavelengths with similar stellar masses.

4.2. SED Properties

In Figure 5, we compare $E(B-V)$, the dust-uncorrected absolute UV magnitude ($M_{\rm FUV}$), and the specific SFR (sSFR; $= {\rm SFR}/{\rm M}_*$) between the ALMA-detected and nondetected SMUVS sources. Here, the histograms for the nondetected sources are weighted according to their stellar masses, as done in Section 4.1. The weights are determined for each redshift bin.

The top two panels in Figure 5 show that the ALMA-detected SMUVS sources tend to have larger dust reddening values than the nondetected sources. Most of the ALMA-detected SMUVS sources have $E(B-V) \geqslant 0.2$ and extend as far as $E(B-V) = 1.0$. As mentioned in Section 3.1, Deshmukh et al. (2018) used the rest-frame *u*–*r* color and $E(B-V)$ to classify SMUVS sources into three populations, namely nondusty star-forming galaxies ($(u-r)_{\rm rest} < 1.3$ and $E(B-V) \leqslant 0.1$), dusty star-forming galaxies ($E(B-V) \geqslant 0.2$), and passive galaxies ($(u-r)_{\rm rest} > 1.3$ and $E(B-V) \leqslant 0.1$). Among the ALMA-detected SMUVS sources, only 4% and 8% are classified as nondusty star-forming galaxies and passive galaxies, respectively. This means that the classification in Deshmukh et al. (2018) works well for the submillimeter bright sources among the SMUVS sources and that LEPHARE appears to retrieve the dusty SEDs of the submillimeter-detected sources successfully, using only optical to IRAC photometry.

We find no clear difference between the $M_{\rm FUV}$ distributions of the ALMA-detected and nondetected sources. As for the sSFR distributions, the sSFRs of the ALMA-detected sources appear to be biased toward higher values with $\log({\rm sSFR\ [yr^{-1}]}) \gtrsim -8$. On the other hand, the nondetected sources cover a wide range of sSFR down to $\log({\rm sSFR\ [yr^{-1}]}) \sim -11$. The lack of a clear difference between the $M_{\rm FUV}$ distributions may partly reflect the fact that galaxies can be fainter in the rest-frame UV because of either stronger dust extinction or lower star formation activity.

The ALMA-detected SMUVS sources are systematically dustier and more active in star formation than the nondetected sources, even after taking into account the difference between the stellar-mass distributions. Such active star formation of the ALMA-detected SMUVS sources would be consistent with their smaller mass-to-light ratios suggested in Section 4.1.

4.3. SMUVS Sources on $\rm M_*$ versus SFR Diagram

Figure 6 shows the M_*–SFR diagram for the ALMA-detected and nondetected SMUVS sources at $z = 2.0$–3.0 and

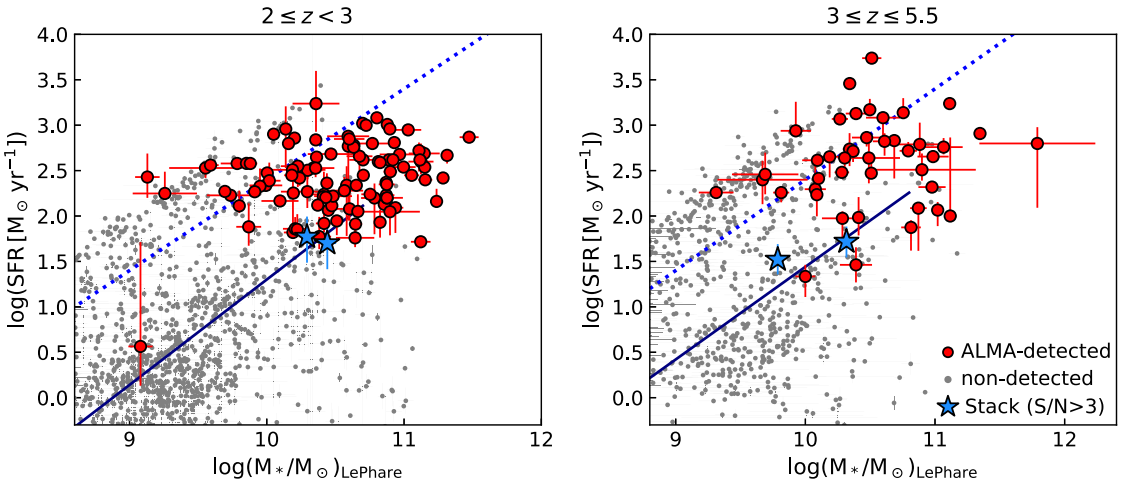

Figure 6. Stellar mass vs. SFR diagram of the SMUVS sources at $z = 2.0$–3.0 (left) and $z = 3.0$–5.5 (right). The stacking results with detection greater than 3σ (Section 3.1) are also shown. The solid line in each panel represents the star-forming main sequence at $z = 2$–3 (left) and at $z = 3$–4 (right) from Santini et al. (2017). The dotted line shows the lower envelope of starburst galaxies defined by Caputi et al. (2021). The ALMA-detected SMUVS sources are located on and above the star-forming main sequence at the epoch.

$z = 3.0$–5.5. The nondetected SMUVS sources appear to show a bimodal distribution on this diagram. One sequence corresponds to the main sequence and the other corresponds to the starburst cloud located above the main sequence (e.g., Rodighiero et al. 2011). Such a bimodal distribution of SMUVS sources on the M_*–SFR diagram was reported by Caputi et al. (2017), using Hα excess galaxies at $3.9 \lesssim z \lesssim 4.9$ selected from the SMUVS catalog based on the photometric excess in IRAC 3.6 μm, and later confirmed by Rinaldi et al. (2022) to extend at all redshifts, $z \sim 3.0$–6.5, with an independent analysis. The definition of starburst galaxies is set to be $\log(\mathrm{sSFR}\,[\mathrm{yr}^{-1}]) \geqslant -7.6$ in Caputi et al. (2017, 2021).

The ALMA-detected SMUVS sources appear distributed across the two sequences, rather than distributed on either the star-forming main sequence or the starburst cloud. They are located at the high-mass end of the distribution of the nondetected SMUVS sources, as shown in Figure 3. The fraction of the ALMA-detected sources classified as starburst at $\log(M_*/M_\odot) \geqslant 9.5$ is 14% at $z = 2.0$–3.0 and 29% at $z = 3.0$–5.5. As for the nondetected SMUVS sources, the starburst fraction at $\log(M_*/M_\odot) \geqslant 9.5$ is 12% at $z = 2.0$–3.0 and 22% at $z = 3.0$–5.5. When we combine the two samples in each redshift bin, the starburst fraction becomes 12% at $z = 2.0$–3.0 and 23% at $z = 3.0$–5.5. The starburst fraction of our sample at $z = 3.0$–5.5 is consistent with the value of 22% obtained for galaxies with $\log(M_*/M_\odot) \geqslant 9.5$ at $z = 3.0$–5.0 in Rinaldi et al. (2022).

In Figure 6, we also show the stacking results with detection greater than 3σ (Table 2). Given the locus of the stacking-detected subsamples on this diagram, these stacking results seem to reflect the physical properties of typical star-forming galaxies at $z = 2.0$–5.5 at the corresponding stellar-mass range.

We calculate the fraction of the dust-obscured star formation ($f_{\mathrm{obscured}} = \mathrm{SFR_{IR}}/\mathrm{SFR_{UV+IR}}$) for these stacking-detected subsamples as well as the individually detected SMUVS sources. Whereas most of the ALMA-detected SMUVS sources have $f_{\mathrm{obscured}} \sim 0.99$ irrespective of their stellar masses, the stacking-detected subsamples have $f_{\mathrm{obscured}} \sim 0.77$–$0.93$. At a given stellar mass, the nondetected SMUVS sources appear to have a smaller contribution from the dust-obscured star formation as compared to the individual detected sources on average. A similar trend is reported by Koprowski et al. (2020) using Lyman Break Galaxies at $3 \leqslant z \leqslant 5$ with and without ALMA detection.

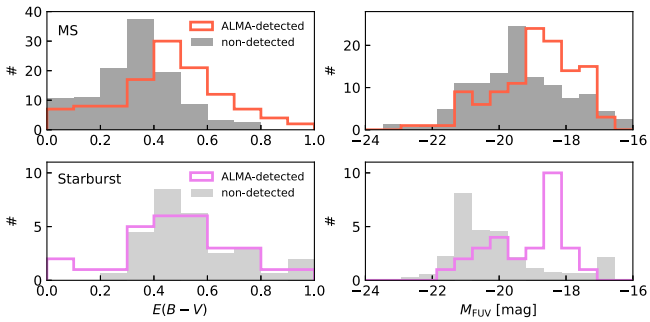

Figure 7. Comparison of $E(B-V)$ (left) and M_{FUV} (right) between the ALMA-detected and nondetected galaxies after dividing the samples into two groups, namely main-sequence galaxies (top) and starburst galaxies (bottom). The nondetected sources are weighted according to their stellar masses. The passive galaxies among the nondetected SMUVS sources are excluded based on the criteria in Deshmukh et al. (2018).

4.4. Starburst Galaxies among SMUVS Sources

Figure 7 shows the comparison of $E(B-V)$ and M_{FUV} between the ALMA-detected and nondetected SMUVS sources at $z = 2.0$–5.5 after dividing the whole sample into two groups, namely main-sequence galaxies and starburst galaxies (Section 4.3). Here we exclude the passive galaxies classified with the Deshmukh et al. (2018) method (Section 3.1). As done in Figures 4 and 5, the nondetected SMUVS sources are weighted according to their stellar masses. The weights are determined for the main-sequence galaxies and starbursts, separately.

As for the main-sequence galaxies, the trend seen in the $E(B-V)$ distributions is similar to what we showed for the whole sample in Figure 5. The difference of the M_{FUV} distributions between the ALMA-detected and nondetected main-sequence galaxies becomes clearer than the case of the whole sample. The top two panels of Figure 7 indicate that the ALMA-detected main-sequence galaxies are fainter in the rest-

frame UV due to their stronger dust extinction. They would be more dust-rich than the nondetected main-sequence galaxies with similar stellar masses. Different submillimeter brightness between the ALMA-detected and nondetected main-sequence galaxies may reflect a variety of dust masses among main-sequence galaxies at a given stellar mass.

As for the starbursts, we find that the ALMA-detected and nondetected starbursts have similar $E(B-V)$ distributions. Furthermore, the nondetected starbursts tend to have larger $E(B-V)$ values than the nondetected main-sequence galaxies. The large $E(B-V)$ values of the nondetected starbursts seem to contradict the fact that they are faint at submillimeter wavelengths. These results may suggest that such nondetected starbursts have higher dust temperature, which leads to fainter submillimeter fluxes at a given IR luminosity. Indeed, it is suggested that active galaxies above the main sequence tend to have higher dust temperatures (e.g., Elbaz et al. 2011; Magnelli et al. 2014; Schreiber et al. 2018). We may see a variety of dust SED shapes among the starbursts at $z > 2$.

5. Summary

We investigated the submillimeter properties of galaxies at $z = 2.0$–5.5 selected with the Spitzer SMUVS survey in the COSMOS field (Ashby et al. 2018; Deshmukh et al. 2018). We crossmatched the SMUVS catalog with the public submillimeter source catalog constructed with ALMA archival data (A^{3}COSMOS; Liu et al. 2019a). We also searched for SMUVS sources that are covered by the ALMA maps but have no counterpart in the A^{3}COSMOS catalog. We then conducted a stacking analysis for the SMUVS sources without ALMA counterparts to investigate their average submillimeter properties.

The ALMA-detected SMUVS sources are systematically massive with $\log(M_{\rm star}/M_{\odot}) \geqslant 10.0$. Furthermore, we find that the ALMA-detected SMUVS sources have systematically redder *Ks*–[4.5] colors (*Ks*–[4.5] $\gtrsim$1.0) than the nondetected sources, even when considering the different stellar-mass distributions between the two samples. The *Ks*–[4.5] color together with the stellar-mass information would be useful to pick up galaxies with bright submillimeter emission at $z > 2$. We also find that the ALMA-detected SMUVS sources tend to have brighter 4.5 μm magnitudes, which may suggest that galaxies with bright submillimeter emission tend to have smaller mass-to-light ratios and thus to be younger than those fainter at submillimeter wavelengths with similar stellar masses.

When comparing the SED properties between the ALMA-detected and nondetected SMUVS sources, we find that the ALMA-detected SMUVS sources tend to have larger $E(B-V)$ values and higher sSFRs. SED fitting with LEPHARE on the optical-to-IRAC photometry retrieves the dusty SEDs of the submillimeter-detected sources at $z > 2$ successfully. The larger dust reddening values of the ALMA-detected SMUVS sources are consistent with the observed redder *Ks*–[4.5] colors.

On the M_*–SFR diagram, the SMUVS sources are distributed across two regions, namely the star-forming main sequence and the starburst cloud (Caputi et al. 2017; Rinaldi et al. 2022). Comparing $E(B-V)$ and $M_{\rm FUV}$ between the ALMA-detected and nondetected main-sequence galaxies, we find that the ALMA-detected main-sequence galaxies have larger $E(B-V)$ values and fainter $M_{\rm FUV}$, which suggests that they are likely more dust-rich than the nondetected main-sequence galaxies with similar stellar masses. We find a different trend for the starburst galaxies. The nondetected starbursts have similar $E(B-V)$ values but brighter $M_{\rm FUV}$ as compared to the ALMA-detected starbursts. This may suggest that the nondetected starbursts have higher dust temperatures and thus become fainter at submillimeter wavelengths, irrespective of their high star formation activity.

High-resolution imaging observation with the James Webb Space Telescope (JWST) will enable us to investigate the rest-frame optical/NIR structures of SMUVS sources at $z > 2$. Obtaining their stellar morphologies and color gradients with multiband images from JWST would lead to further investigation into what causes the difference between the ALMA-detected and nondetected sources or the difference between the main-sequence galaxies and starbursts at a given stellar mass. The widefield observations with NIRCam and MIRI are now being conducted in the COSMOS field (COSMOS-Web; Casey et al. 2023). The NIRCam imaging data in four filters covering 0.54 deg^2 will become available once the program has been completed, and this will be a useful data set for SMUVS sources.

Acknowledgments

We would like to thank the anonymous referee for a careful reading and constructive comments that improved the clarity of this paper. T.L.S. would like to thank John Silverman and Chris Hayward for helpful comments and suggestions. This work was performed with the support of the Canon Foundation in Europe. K.C. and S.v.M. acknowledge funding from the European Research Council through the award of the Consolidator Grant ID 681627-BUILDUP. Kavli IPMU is supported by the World Premier International Research Center Initiative (WPI), MEXT, Japan.

This paper makes use of the following ALMA data: ADS/JAO.ALMA#2011.0.00064.S, ADS/JAO.ALMA#2011.0.00097.S, ADS/JAO.ALMA#2011.0.00539.S, ADS/JAO.ALMA#2012.1.00076.S, ADS/JAO.ALMA#2012.1.00323.S, ADS/JAO.ALMA#2012.1.00523.S, ADS/JAO.ALMA#2012.1.00536.S, ADS/JAO.ALMA#2012.1.00978.S, ADS/JAO.ALMA#2013.1.00034.S, ADS/JAO.ALMA#2013.1.00118.S, ADS/JAO.ALMA#2013.1.00151.S, ADS/JAO.ALMA#2013.1.00208.S, ADS/JAO.ALMA#2013.1.00884.S, ADS/JAO.ALMA#2013.1.01258.S, ADS/JAO.ALMA#2013.1.01292.S, ADS/JAO.ALMA#2015.A.00026.S, ADS/JAO.ALMA#2015.1.00055.S, ADS/JAO.ALMA#2015.1.00137.S, ADS/JAO.ALMA#2015.1.00207.S, ADS/JAO.ALMA#2015.1.00260.S, ADS/JAO.ALMA#2015.1.00379.S, ADS/JAO.ALMA#2015.1.00388.S, ADS/JAO.ALMA#2015.1.00540.S, ADS/JAO.ALMA#2015.1.00568.S, ADS/JAO.ALMA#2015.1.00664.S, ADS/JAO.ALMA#2015.1.00704.S, ADS/JAO.ALMA#2015.1.00928.S, ADS/JAO.ALMA#2015.1.01074.S, ADS/JAO.ALMA#2015.1.01105.S, ADS/JAO.ALMA#2015.1.01111.S, ADS/JAO.ALMA#2015.1.01171.S, ADS/JAO.ALMA#2015.1.01212.S, ADS/JAO.ALMA#2015.1.01495.S, ADS/JAO.ALMA#2016.1.00171.S, ADS/JAO.ALMA#2016.1.00279.S, ADS/JAO.ALMA#2016.1.00478.S, ADS/JAO.ALMA#2016.1.00804.S, ADS/JAO.ALMA#2016.1.01040.S, and ADS/JAO.ALMA#2016.1.01208.S.

ALMA is a partnership of ESO (representing its member states), NSF (USA), and NINS (Japan), together with NRC

(Canada), MOST and ASIAA (Taiwan), and KASI (Republic of Korea), in cooperation with the Republic of Chile. The Joint ALMA Observatory is operated by ESO, AUI/NRAO, and NAOJ.

Software: MAGPHYS (da Cunha et al. 2008), LEPHARE (Arnouts et al. 1999; Ilbert et al. 2006), TOPCAT (Taylor 2005), Astropy (Astropy Collaboration 2013; Price-Whelan et al. 2018), DAOPHOT (Stetson 1987), IRAF (Tody 1986, 1993).

ORCID iDs

Tomoko L. Suzuki https://orcid.org/0000-0002-3560-1346
Sophie E. van Mierlo https://orcid.org/0000-0001-8289-2863
Karina I. Caputi https://orcid.org/0000-0001-8183-1460

References

Algera, H. S. B., Inami, H., Oesch, P. A., et al. 2023, MNRAS, 518, 6142
An, F. X., Simpson, J. M., Smail, I., et al. 2019, ApJ, 886, 48
An, F. X., Stach, S. M., Smail, I., et al. 2018, ApJ, 862, 101
Aravena, M., Boogaard, L., Gónzalez-López, J., et al. 2020, ApJ, 901, 79
Arnouts, S., Cristiani, S., Moscardini, L., et al. 1999, MNRAS, 310, 540
Ashby, M. L. N., Caputi, K. I., Cowley, W., et al. 2018, ApJS, 237, 39
Ashby, M. L. N., Caputi, K. I., Cowley, W., et al. 2020, Spitzer Matching Survey of the Ultra-VISTA Deep Stripes, IPAC, doi:10.26131/IRSA401
Astropy Collaboration, Robitaille, T. P., Tollerud, E. J., et al. 2013, A&A, 558, A33
Barger, A. J., Cowie, L. L., Sanders, D. B., et al. 1998, Natur, 394, 248
Battisti, A. J., Cunha, E. d., Shivaei, I., & Calzetti, D. 2020, ApJ, 888, 108
Battisti, A. J., da Cunha, E., Grasha, K., et al. 2019, ApJ, 882, 61
Bouwens, R. J., Aravena, M., Decarli, R., et al. 2016, ApJ, 833, 72
Bruzual, G., & Charlot, S. 2003, MNRAS, 344, 1000
Burgarella, D., Buat, V., Gruppioni, C., et al. 2013, A&A, 554, A70
Calzetti, D., Armus, L., Bohlin, R. C., et al. 2000, ApJ, 533, 682
Caputi, K. I., Caminha, G. B., Fujimoto, S., et al. 2021, ApJ, 908, 146
Caputi, K. I., Deshmukh, S., Ashby, M. L. N., et al. 2017, ApJ, 849, 45
Casey, C. M., Kartaltepe, J. S., Drakos, N. E., et al. 2023, ApJ, 954, 31
Chabrier, G. 2003, PASP, 115, 763
Charlot, S., & Fall, S. M. 2000, ApJ, 539, 718
Chen, C.-C., Smail, I., Ivison, R. J., et al. 2016, ApJ, 820, 82
Civano, F., Marchesi, S., Comastri, A., et al. 2016, ApJ, 819, 62
Comparat, J., Richard, J., Kneib, J.-P., et al. 2015, A&A, 575, A40
COSMOS Project 2020, Cosmic Evolution Survey with HST, IPAC, doi:10.26131/IRSA178
da Cunha, E., Charlot, S., & Elbaz, D. 2008, MNRAS, 388, 1595
da Cunha, E., Walter, F., Smail, I. R., et al. 2015, ApJ, 806, 110
Deshmukh, S., Caputi, K. I., Ashby, M. L. N., et al. 2018, ApJ, 864, 166
Dudzevičiūtė, U., Smail, I., Swinbank, A. M., et al. 2020, MNRAS, 494, 3828
Dunlop, J. S., McLure, R. J., Biggs, A. D., et al. 2017, MNRAS, 466, 861
Efron, B. 1982, The Jackknife, the Bootstrap and Other Resampling Plans (Philadelphia, PA: SIAM)
Elbaz, D., Dickinson, M., Hwang, H. S., et al. 2011, A&A, 533, A119
Fazio, G. G., Hora, J. L., Allen, L. E., et al. 2004, ApJS, 154, 10
Franco, M., Elbaz, D., Zhou, L., et al. 2020, A&A, 643, A30
Fudamoto, Y., Oesch, P. A., Magnelli, B., et al. 2020, MNRAS, 491, 4724
Hasinger, G., Capak, P., Salvato, M., et al. 2018, ApJ, 858, 77
Hodge, J. A., & da Cunha, E. 2020, RSOS, 7, 200556
Hodge, J. A., Karim, A., Smail, I., et al. 2013, ApJ, 768, 91
Hughes, D. H., Serjeant, S., Dunlop, J., et al. 1998, Natur, 394, 241
Ilbert, O., Arnouts, S., McCracken, H. J., et al. 2006, A&A, 457, 841
Inoue, A. K., Shimizu, I., Iwata, I., et al. 2014, MNRAS, 442, 1805
Jin, S., Daddi, E., Liu, D., et al. 2018, ApJ, 864, 56
Kennicutt, Robert C. , J. 1998, ApJ, 498, 541
Koprowski, M. P., Coppin, K. E. K., Geach, J. E., et al. 2020, MNRAS, 492, 4927
Kriek, M., Shapley, A. E., Reddy, N. A., et al. 2015, ApJS, 218, 15
Laigle, C., McCracken, H. J., Ilbert, O., et al. 2016, ApJS, 224, 24
Le Fèvre, O., Tasca, L. A. M., Cassata, P., et al. 2015, A&A, 576, A79
Lilly, S. J., Le Fèvre, O., Renzini, A., et al. 2007, ApJS, 172, 70
Liu, D., Daddi, E., Dickinson, M., et al. 2018, ApJ, 853, 172
Liu, D., Lang, P., Magnelli, B., et al. 2019, ApJS, 244, 40
Madau, P., & Dickinson, M. 2014, ARA&A, 52, 415
Magnelli, B., Lutz, D., Saintonge, A., et al. 2014, A&A, 561, A86
McCracken, H. J., Milvang-Jensen, B., Dunlop, J., et al. 2012, A&A, 544, A156
Michałowski, M. J., Dunlop, J. S., Koprowski, M. P., et al. 2017, MNRAS, 469, 492
Michałowski, M. J., Hayward, C. C., Dunlop, J. S., et al. 2014, A&A, 571, A75
Miettinen, O., Delvecchio, I., Smolčić, V., et al. 2017, A&A, 606, A17
Oke, J. B., & Gunn, J. E. 1983, ApJ, 266, 713
Price-Whelan, A. M., Sipőcz, B. M., Günther, H. M., et al. 2018, AJ, 156, 123
Rinaldi, P., Caputi, K. I., van Mierlo, S. E., et al. 2022, ApJ, 930, 128
Rodighiero, G., Daddi, E., Baronchelli, I., et al. 2011, ApJL, 739, L40
Santini, P., Fontana, A., Castellano, M., et al. 2017, ApJ, 847, 76
Schinnerer, E., Groves, B., Sargent, M. T., et al. 2016, ApJ, 833, 112
Schreiber, C., Elbaz, D., Pannella, M., et al. 2018, A&A, 609, A30
Scoville, N., Aussel, H., Brusa, M., et al. 2007, ApJS, 172, 1
Scoville, N., Sheth, K., Aussel, H., et al. 2016, ApJ, 820, 83
Smail, I., Ivison, R. J., & Blain, A. W. 1997, ApJL, 490, L5
Stetson, P. B. 1987, PASP, 99, 191
Tadaki, K.-i., Belli, S., Burkert, A., et al. 2020, ApJ, 901, 74
Takeuchi, T. T., Buat, V., & Burgarella, D. 2005, A&A, 440, L17
Taniguchi, Y., Scoville, N., Murayama, T., et al. 2007, ApJS, 172, 9
Taylor, M. B. 2005, in ASP Conf. Ser. 347 Astronomical Data Analysis Software and Systems XIV,, ed. P. Shopbell, M. Britton, & R. Ebert (San Francisco, CA: ASP), 29
Tody, D. 1986, Proc. SPIE, 627, 733
Tody, D. 1993, Asdass II, 52, 173
van Mierlo, S. E., Caputi, K. I., Ashby, M., et al. 2022, A&A, 666, A200
Wang, T., Elbaz, D., Schreiber, C., et al. 2016, ApJ, 816, 84
Wang, W.-H., Barger, A. J., & Cowie, L. L. 2012, ApJ, 744, 155
Werner, M. W., Roellig, T. L., Low, F. J., et al. 2004, ApJS, 154, 1
Wuyts, S., Förster Schreiber, N. M., Lutz, D., et al. 2011, ApJ, 738, 106
Yamaguchi, Y., Kohno, K., Hatsukade, B., et al. 2020, PASJ, 72, 69
Zavala, J. A., Casey, C. M., Manning, S. M., et al. 2021, ApJ, 909, 165